Seismic scattering and absorption properties of Mars estimated through coda analysis on a long-period surface wave of S1222a marsquake

Keisuke Onodera[1], Takuto Maeda[2], Kiwamu Nishida[1], Taichi Kawamura[3]
Ludovic Margerin[4], Sabrina Menina[3], Philippe Lognonné[3]
William Bruce Barnedt[5]

[1]Earthquake Research Institute, The University of Tokyo, Tokyo, Japan
[2]Graduate School of Science and Technology, Hirosaki University, Hirosaki, Aomori, Japan
[3]Université Paris Cité, Institut de Physique du Globe de Paris, CNRS, Paris, France
[4]Institut de Recherche en Astrophysique et Planétologie, Université Toulouse III Paul Sabatier, CNRS, CNES, Toulouse, France.
[5]Jet Propulsion Laboratory, California Institute of Technology, California, USA

Key Points:

- We modeled the scattering effect of the largest marsquake (S1222a) using radiative transfer theory on a spherical Mars.
- The inversion revealed that the intrinsic and scattering quality factors below 0.1 Hz were 1000 – 1500 and 30 – 500, respectively.
- We summarized the Martian quality factors derived so far and found that they are relatively Earth-like rather than Moon-like.

Corresponding author: Keisuke Onodera, onodera@eri.u-tokyo.ac.jp

Abstract

On May 4th 2022, the seismometer on Mars observed the largest marsquake (S1222a) during its operation. One of the most specific features of S1222a is the long event duration lasting more than 8 hours from the occurrence, in addition to the clear appearance of body and surface waves. As demonstrated on Earth, by modeling a long-lasting and scattered surface wave with the radiative transfer theory, we estimated the scattering and intrinsic quality factors of Mars (Q_s and Q_i). This study especially focused on the frequency range between 0.05 – 0.09 Hz, where Q_s and Q_i have not been constrained yet. Our results revealed that $Q_i = 1000 - 1500$ and $Q_s = 30 - 500$. By summarizing the Martian Q_i and Q_s estimated so far and by comparing them with those of other celestial bodies, we found that, overall, the Martian scattering and absorption properties showed Earth-like values.

Plain Language Summary

Since February 2019, NASA's InSight (Interior Exploration using Seismic Investigations, Geodesy, and Heat Transport) has been conducting quasi-continuous seismic observation for more than three years. The seismic data from Mars has contributed significantly to a better understanding of the interior structure and the seismicity of the red planet. On May 4th 2022 (1222 Martian days after landing), another key event occurred, called S1222a. The event showed the largest seismic moment release (magnitude 4.7) and extremely long duration (> 8 hours) with intense seismic scattering. As demonstrated on Earth, the long-lasting scattered waves are useful for retrieving information about the structural heterogeneity within a planet. In this study, by applying the radiative transfer theory — which considers the energy transportation from the seismic source to the observation point — to Mars, we evaluated the energy decay rate due to seismic scattering and energy absorption by a medium. By comparing our results with those of other solid bodies, we found that the Martian scattering and absorption features were closer to the terrestrial ones than to the lunar ones.

1 Introduction

After almost three years of seismic observations on Mars, the seismometer installed by Interior Exploration using Seismic Investigations, Geodesy, and Heat Transport (InSight) detected a magnitude 4.7 class event on Sol 1222 (1222 Martian days after landing). Following the convention of Marsquake Service (MQS), this event was labeled as S1222a (Kawamura et al., 2022).

InSight deployed two types of seismometers: the Very Broadband seismometer (VBB) covering from a 0.01 – 10 Hz frequency band, and the Short-Period seismometer (SP) covering from 1 – 50 Hz [e.g., Lognonné et al. (2019)]. Quasi-continuous observations since 2019 brought us new insights into the Martian seismicity and internal structure [e.g., Lognonné et al. (2020); Banerdt et al. (2020); Giardini et al. (2020); Khan et al. (2021); Knapmeyer-Endrun et al. (2021); Stähler et al. (2021)].

As described by Kawamura et al. (2022), only VBB was operated on Sol 1222 due to the severe power supply conditions. That is, this event is only available for VBB (the channel names are XB.ELYSE.02.[BHU, BHV, and BHW], for instance). The remarkable characteristics of S1222a are, in addition to clear P- and S-wave arrivals, the excitation of both Rayleigh and Love waves, which are rarely observed in other marsquakes [Kawamura et al. (2022), Kim et al. (2022)]. Figures 1a-c show an example of the time series of S1222a. From top to bottom, followed by the spectrogram, the mean squared envelope (MS envelope), and the waveform filtered at 0.05 – 0.09 Hz are shown. Interestingly, the low-frequency energy lasts approximately 8 hours from the arrival (e.g., Figure 1b). The gradual decrease from the energy peak is called the coda. In terrestrial seis-

mology, it is known that the coda waves are generated due to the heterogeneous structures within a planet [e.g., Aki (1969); Aki and Chouet (1975)].

In this study, to constrain the scattering and attenuation properties of the Martian lithosphere, we focus on the decay coda part at a frequency of 0.05 – 0.09 Hz, where Rayleigh wave is strongly excited, and the contamination of glitches is smaller than that of lower frequencies ($<$ 0.05 Hz). As these parameters have been poorly constrained at that frequency, our study fills the missing piece regarding the heterogeneous structures of Mars. Because the inhomogeneous structure of a planet strongly reflects the evolution processes in the past, understanding the heterogeneous structure would be one of the paramount steps toward revealing the history of Mars.

In the following, we will review the Rayleigh wave features of S1222a, introduce how to retrieve the scattering and attenuation parameters from the decay coda, and then show the inversion results. Finally, we compare the intrinsic and scattering attenuation properties between the Earth, the Moon, and Mars.

2 The observed Rayleigh wave and its multi-orbital phases

In Figures 1b-c, the Rayleigh wave arrival (R_1), which was identified by Kawamura et al. (2022), is shown by the red filled area. The expected arrival times of Rayleigh wave traveling along the major arc (R_2) and the multi-orbital phases (R_3, R_4, and R_5) are shown by the green and red-filled areas. See Figures 1d-e and the caption for the description of the multi-orbital phases of Rayleigh waves and their group velocity. At first glance, the phases following R_1 are not clearly seen in our target frequency range. To confirm whether such phases are present in the data, we performed a simple demonstration, as described below.

If the Rayleigh wave component is excited, there must be a $\pi/2$ phase shift between the vertical and radial seismic records. In other words, the multiplication of the vertical ground velocity $V_z(t)$ and the Hilbert-transformed radial velocity $\mathcal{H}[V_r(t)]$ should return the one-sided signal during the arrival of the Rayleigh wave components (e.g., the positive signal for R_1, R_3, R_5 and the negative signal for R_2 and R_4). Figure 1f shows an example of Rayleigh wave detection. Around 0.2 h lapse time (R_1 arrival), the positive one-sided signal lasts for approximately 10 min, indicating that the Rayleigh wave component arrives during this period. On the other hand, looking at Figures 1g-h, it is difficult to find Rayleigh wave-related phases because of the low signal-to-noise ratio. In other words, the scattering effect seems strong enough to attenuate both R_2 and the multi-orbital phases to the level of other incoherent signals, at least in our target frequency range (0.05 – 0.09 Hz). This is consistent with the report by Kawamura et al. (2022), who could not confirm these phases in this frequency range, either.

3 Radiative transfer modeling on a spherical Mars

In terrestrial seismology, the radiative transfer theory has been used to investigate the heterogeneous structures [e.g., Aki and Chouet (1975); Sato (1977); Wu (1985)]. Recently, Menina et al. (2021) and Karakostas et al. (2021) applied this approach to Mars and estimated the scattering and attenuation properties. To further advance our understanding of this topic, we will investigate the scattering and attenuation properties at a lower frequency ($<$ 0.1 Hz) than before, utilizing the scattering features observed in S1222a.

In the following analysis, we consider a sphere with a Martian radius $R = 3389.5$ km on the spherical coordinate system, where the seismic source (S1222a) and a receiver (InSight SEIS) are located on (3.0°S, 171.9°E) and (4.502°N, 135.623°E), respectively (Golombek et al., 2020; Kawamura et al., 2022). From a source to receiver, the distance along the

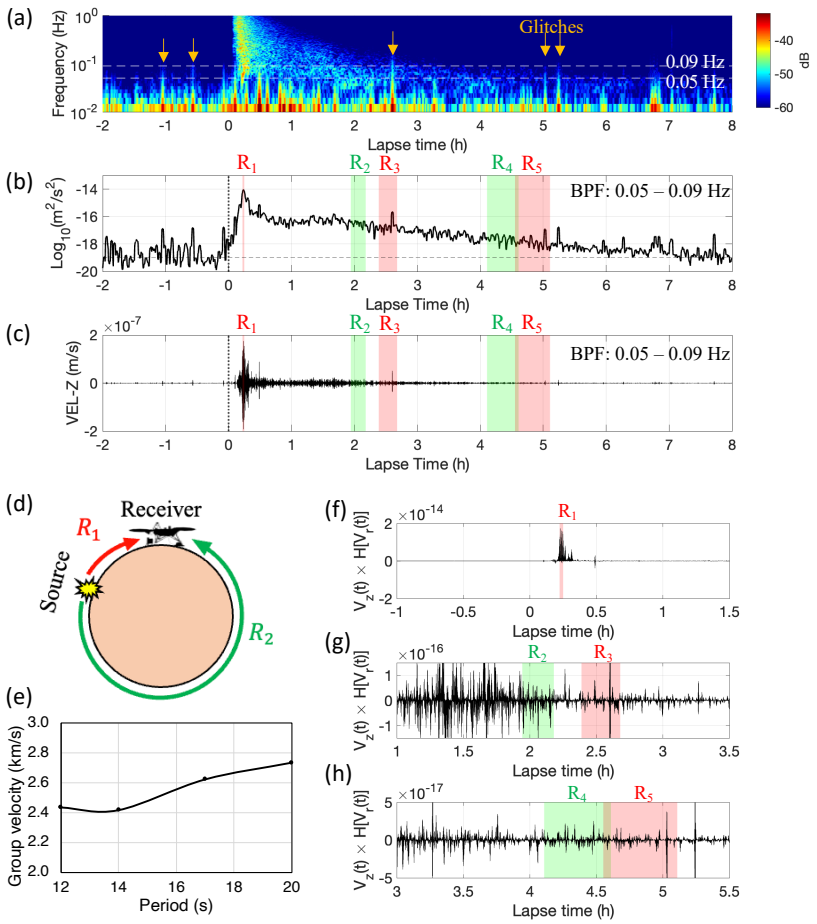

Figure 1. (a) Spectrogram of the VBB vertical component. The horizontal axis represents the lapse time in hours from the origin time, and the vertical axis shows frequency covering from 10^{-2} to 1 Hz. The orange arrows show the representative glitches seen in this time period. (b) Mean squared (MS) envelope at the low-frequency band. The deglitched waveform data (see the text) was bandpass filtered between 0.05 and 0.09 Hz, and the squared time series were smoothed with a time window of 100 s with 50% overlap. The red line tagged R_1 shows the R_1 arrival read by Kawamura et al. (2022). The red and green filled areas show the expected arrival times of the multi-orbital phases (R_2, R_3, ...), which are computed based on the group velocity shown in (e). The horizontal broken line shows the noise level estimated with the median value before the origin time, which is consistent with the representative noise level for this period of the sol (Figure S1). (c) The vertical-component waveform filtered between 0.05 and 0.09 Hz. The vertical lines and filled areas are the same as in (b). (d) Schematic diagram of Rayleigh wave propagation on a spherical Mars surface. R_1 refers to the Rayleigh wave propagating along the minor arc, and R_2 refers to that traveling along the major arc. The subscript number increases by two as the Rayleigh wave goes around Mars (i.e., R_3, R_5... for minor arc direction). (e) The dispersion curve for the group velocity as a function of period. (f)-(h) Time series of $V_z(t) \times \mathcal{H}[V_r(t)]$ at 0.05 – 0.09 Hz band for the time window of -1 – 1.5 h, 1 – 3.5 h, and 3 – 5.5 h lapse time, respectively. The red and green areas show the expected arrival times of Rayleigh wave components as in (b) and (c).

minor arc θ and the forward azimuth ϕ are measured as shown in Figure 2a. According to Kawamura et al. (2022), $\theta = 37 \pm 1.6°$ and $\phi = 281 \pm 11°$. The last scattering point — where the seismic wave radiated from the source encounters before the arrival at the receiver — is apart from the source with the distance and the forward azimuth being θ' and ϕ'. Under this geometry setting, let us consider the energy density of the fundamental-mode Rayleigh wave for (i) the direct wave component, (ii) the single-scattered component, and (iii) the multiple-scattered component to model the observed MS envelope.

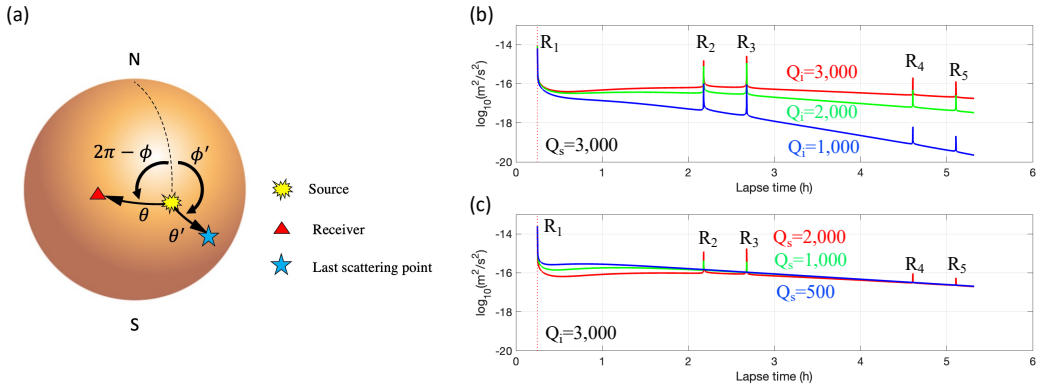

Figure 2. (a)Geometry of a source, receiver, and the last scattering point on a spherical body. (b) Comparison of theoretical MS envelopes for the different intrinsic quality factors (Q_i=1000, 2000, and 3000) with Q_s fixed to 3000. (c) Comparison of theoretical MS envelopes for the different scattering quality factors (Q_s=500, 1000, and 2000) with Q_i fixed to 3000.

Following Sato and Nohechi (2001), the energy density of Rayleigh waves propagating along the minor and major arcs on a spherical planet can be written as:

$$E^0(\theta,\phi,t) = \frac{W\Phi(\phi)}{2\pi R^2 \sin\theta} \sum_{n=0}^{\infty} \left[\delta\left(\frac{Vt}{R} - \theta - 2\pi n\right) + \delta\left(\frac{Vt}{R} + \theta - 2\pi(n+1)\right)\right], \quad (1)$$

where t is the time, W is the scaled energy factor, V is the group velocity, and δ is the delta function. Φ denotes the radiation pattern of the source. Because of the large uncertainty in the focal mechanism with a single-spot observation, we assumed the isotropic radiation for Φ as:

$$\Phi = \frac{1}{2\pi}. \quad (2)$$

Normalizing the energy density with $W/4\pi R^2$ and introducing the intrinsic and scattering attenuation factors yields the scaled energy density of the direct wave component ϵ^0:

$$\epsilon^0(\theta,t;\omega) = \frac{2\Phi}{\sin\theta} \sum_{n=0}^{\infty} \left[\delta\left(\frac{Vt}{R} - \theta - 2\pi n\right) + \delta\left(\frac{Vt}{R} + \theta - 2\pi(n+1)\right)\right] e^{-(Q_s^{-1}+Q_i^{-1})\omega t}, \quad (3)$$

where ω is the angular frequency, and Q_s and Q_i are the scattering and intrinsic attenuation factors, respectively.

As demonstrated for earthquakes (Sato & Nohechi, 2001; Sato & Nishino, 2002; Maeda et al., 2006), the energy density of single-scattered Rayleigh wave ϵ^S can be expressed as:

$$\epsilon^S(\theta,\phi,t;\omega) = \frac{\omega R}{\pi V Q_s} e^{-(Q_s^{-1}+Q_i^{-1})\omega t} \int_0^{2\pi} d\phi' \frac{\Phi n_s(\theta,t)}{\sqrt{(\sin\tau - \sin\theta\cos(\phi-\phi'))^2 + (\cos\theta - \cos\tau)^2}}, \quad (4)$$

where $\tau = Vt/R$, and the multiple orbit factor n_s is given by:

$$n_s(\theta, t) = \begin{cases} 0 & (\tau < \theta), \\ 1 & (\theta < \tau < 2\pi - \theta), \\ 2 & (2\pi - \theta < \tau < 2\pi + \theta), \\ 3 & (2\pi + \theta < \tau < 4\pi - \theta), \\ 4 & (4\pi - \theta < \tau < 4\pi + \theta), \\ ... \end{cases} \tag{5}$$

To calculate the multiple scattering term, we use the asymptotic form, which has been validated as a good approximation for earthquakes (Sato & Nishino, 2002). The energy density of the multiple scattering term ϵ^M can be written as:

$$\epsilon^M(t;\omega) = \left(1 - e^{-\frac{\omega t}{Q_s}} - \frac{\omega t}{Q_s} e^{-\frac{\omega t}{Q_s}}\right) e^{-\frac{\omega t}{Q_i}}. \tag{6}$$

By combining all three terms above, we can theoretically draw the MS envelopes as follows:

$$E(\theta, \phi, t; \omega) = \frac{W}{4\pi R^2}[\epsilon^0(\theta, t; \omega) + \epsilon^S(\theta, \phi, t; \omega) + \epsilon^M(t; \omega)]. \tag{7}$$

Because the scaled energy factor W is unknown, we focus on the relative (or normalized) MS envelope and first evaluate the intrinsic and scattering quality factors, and then estimate W using the preferable quality factors (See Sections 5 and 6).

To clarify how Q_i and Q_s affect the envelope shape, Figures 2b-c show examples of the theoretical envelopes. Q_i mostly controls the energy decay rate, and Q_s determines the peak intensity of Rayleigh waves.

4 Target frequencies and data processing

We limit ourselves to studying the frequency range below 0.1 Hz, where the scattering and intrinsic quality factors have not been constrained yet. Especially we processed the data at the four frequencies: 1/12, 1/14, 1/17, and 1/20 Hz.

To reduce the contamination by glitches, we used the data denoised with the method proposed by Scholz et al. (2020). For preprocessing, we performed (i) detrending and demeaning, (ii) applying pre-filtering between 0.005 and 9.5 Hz, and (iii) correcting the instrumental response to convert the raw data into particle velocity. Then, the time trace was bandpass filtered using the 4th order Butterworth filter with the corner frequencies of $0.9f_c$ and $1.1f_c$, where f_c is the center frequency (1/12, 1/14, 1/17, and 1/20 Hz). As we focus on Rayleigh wave and stand on the approach by Sato and Nishino (2002), we used the vertical component of VBB in the analysis.

5 Inversion with grid search method

In the inversion process, we used the MS envelope normalized with an average value between 1.5 and 3.5 h lapse time for the respective frequency bands. In other words, we modeled the relative decay trend to obtain the scattering and intrinsic quality factors.

A grid search concerning the scattering quality factor Q_s and the intrinsic quality factor Q_i was conducted. We varied the Q_s and Q_i in a range of 200 – 4000 and 500 – 5000, respectively. The parameter ranges were equally divided into 20 on a log scale. The goodness of fit was evaluated with the summation of squared residual value σ, as follows:

$$\sigma_{j,k}(f_c) = \Sigma_{t_{min}}^{t_{max}} \left[\log_{10}\left(\frac{S^{\mathrm{obs}}(t; f_c)}{S_{j,k}^{\mathrm{rtf}}(t; f_c)}\right)\right]^2, \tag{8}$$

where t_{min} (= 1.5 h) and t_{max} (= 3.5 h) define the time window for the fitting, $S^{\rm obs}$ and $S^{\rm rtf}$ are the MS envelopes for the observation and the theoretical curve (scaled with the average value in the time window). The subscripts j and k in Equation 8 are for the varied Q_i and Q_s parameters. When $j = 1$ and $k = 1$, $Q_i = 500$ and $Q_s = 200$.

6 Estimated intrinsic and scattering quality factors and scaled energy factor

Figure 3a presents the inversion results for the respective frequencies. The color map indicates the distribution of the residual values in the Q_i–Q_s parameter space, where the blue color indicates smaller residual values. Figure 3b displays the best-fitted curves for each frequency band (all calculated curves can be found in Figure S2). Looking at the residual map, Q_i is well constrained, whereas any Q_s can provide good fits as long as Q_i is in the range of 1000 – 1500. As demonstrated in Figures 2b-c, Q_i mostly controls the gradient of the decay coda, whereas Q_s affects the peak intensity of Rayleigh wave and its multi-orbital phases. Thus, it is reasonable that Q_i is more easily constrained than Q_s.

To better constrain Q_s, we performed an additional analysis considering that R_2 and the multi-orbital phases were attenuated and could not be confirmed within our target frequency range (Section 2). Figure 4 shows the examples of parameter studies on Q_s with Q_i fixed to the best-fitted value in the previous inversion. In Figures 4a-b, comparing the first and the second rows gives us the upper limit of Q_s, which provides the smallest scattering intensity to hide the peaks of R_2 and the multi-orbital phases under the multiple scattering effects. In turn, Figures 4c-d provides us with the lower limit of Q_s which is the smallest scattering intensity to diffuse the R_1 peak completely. Consequently, we found that Q_s ranged from 60 to 500 for 1/12 and 1/14 Hz and from 30 to 350 for 1/17 and 1/20 Hz, respectively (Figure 4 and Figure S3). It appears that Q_s depends on the frequency. However, this cannot be concluded because both Q_s-ranges return similar residual values. Therefore, we conclude that the plausible Q_s range is 30 – 500.

Together with the estimated Q_i and Q_s, we evaluated the scaled energy factor W. As shown in Figure S4, we calculated the summation of residual for each frequency band in the same manner as in Equation 8 and found a preferable W value of $(8.5 \pm 1.5) \times 10^{-9}$ $(\mathrm{m/s})^2 \cdot \mathrm{km}^2$.

7 Intrinsic and scattering quality factors of the Earth, the Moon, and Mars

In this section, to compare the scattering and attenuation properties with the same criteria between the Earth, the Moon, and Mars, we review Q_i and Q_s derived thus far on each body. If previous studies provided different parameters, such as diffusivity or correlation length, we converted them into Q_i and Q_s. Because of a large uncertainty in the depth and thickness of the Martian scattering layer, a detailed discussion of the structures cannot be put forward. Instead, we limit ourselves to showing the comparative figures for Q_i and Q_s against frequency and giving a preliminary interpretation.

7.1 Earth

Figures 5a-b show the intrinsic and scattering quality factors for the Earth, the Moon, and Mars, respectively, where the quality factors for body waves are displayed above 0.1 Hz, and those for surface waves are presented below 0.1 Hz.

The Earth's lithosphere Q_i and Q_s are estimated through the radiative transfer theory for isotropic single and/or multiple scattering models, using S-wave scattered waves

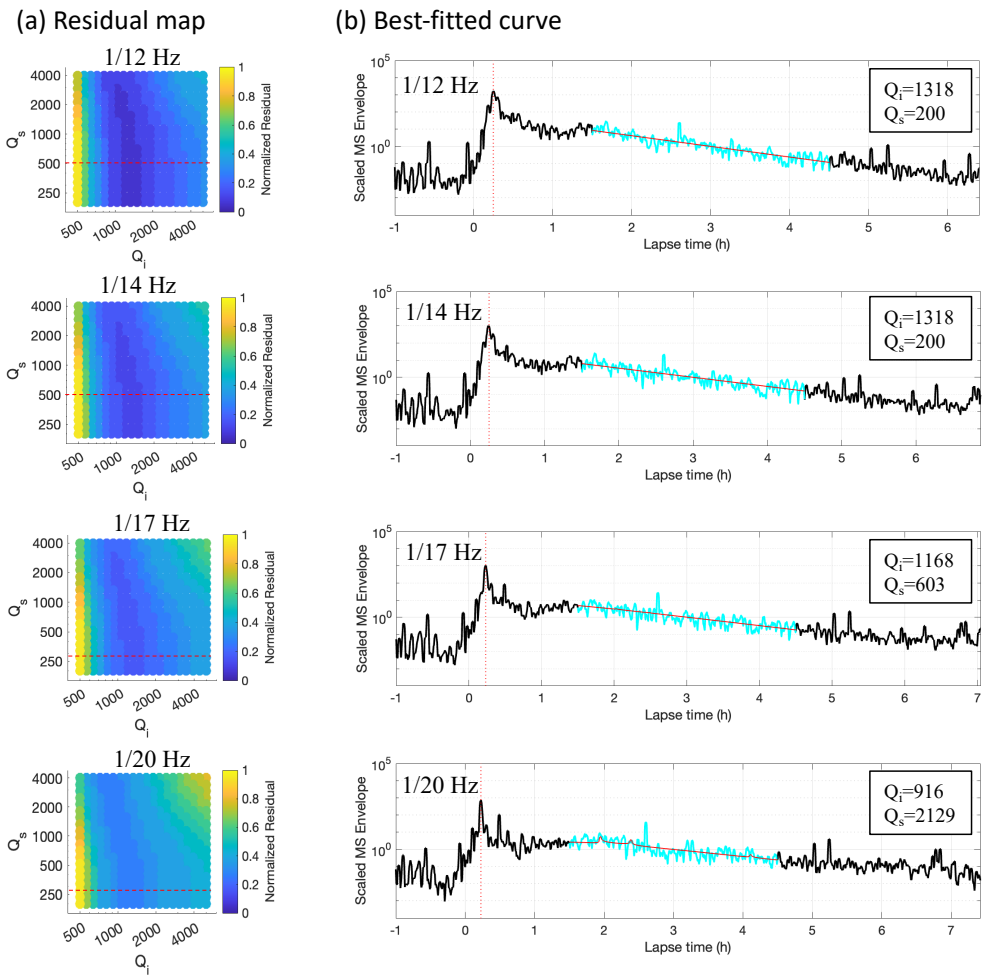

Figure 3. (a) Grid search results for the respective frequency bands (1/12 Hz through 1/20 Hz from the top to bottom). The horizontal axis shows the intrinsic Q, and the vertical axis shows the scattering Q. The color map represents the summation of the squared residual (Equation 8), which is normalized with the maximum value. The red dashed line shows the upper limit of the scattering Q (See the text for the details). (b) The best-fitted curves superposed on the observations. For the fitting, the cyan profiles (1.5 – 4.5 h window) were used out of the entire MS envelopes. The amplitude is normalized with the average value within the time window of 1.5 – 4.5 h. The red profiles show the best-fitted curves. Note that the theoretical curves in red were move averaged in the same way as the observation in black.

of local earthquakes. The lithosphere's Q_i and Q_s for body waves in Figures 5a-b were taken from the recent reviews by Sato et al. (2012) and Sato (2019). Both quality factors show frequency dependence. Q_i ranges 30 – 500 at 2 Hz and 250 – 5000 at 20 Hz. Q_i for surface waves was computed using Mineos [Masters et al. (2011)] with the Preliminary Earth model [PREM; Dziewonski and Anderson (1981)]. The upper limit ($\sim$ 900) corresponds to the lithosphere. The value decreases with decreasing frequency because Rayleigh wave at a lower frequency becomes more sensitive to the deeper part: the asthenospheric structure. The Q_s at 0.01 Hz ($\sim$ 10000) was estimated by Sato and Nohechi (2001) analyzing the Rayleigh wave and its multiple orbits as performed in this study.

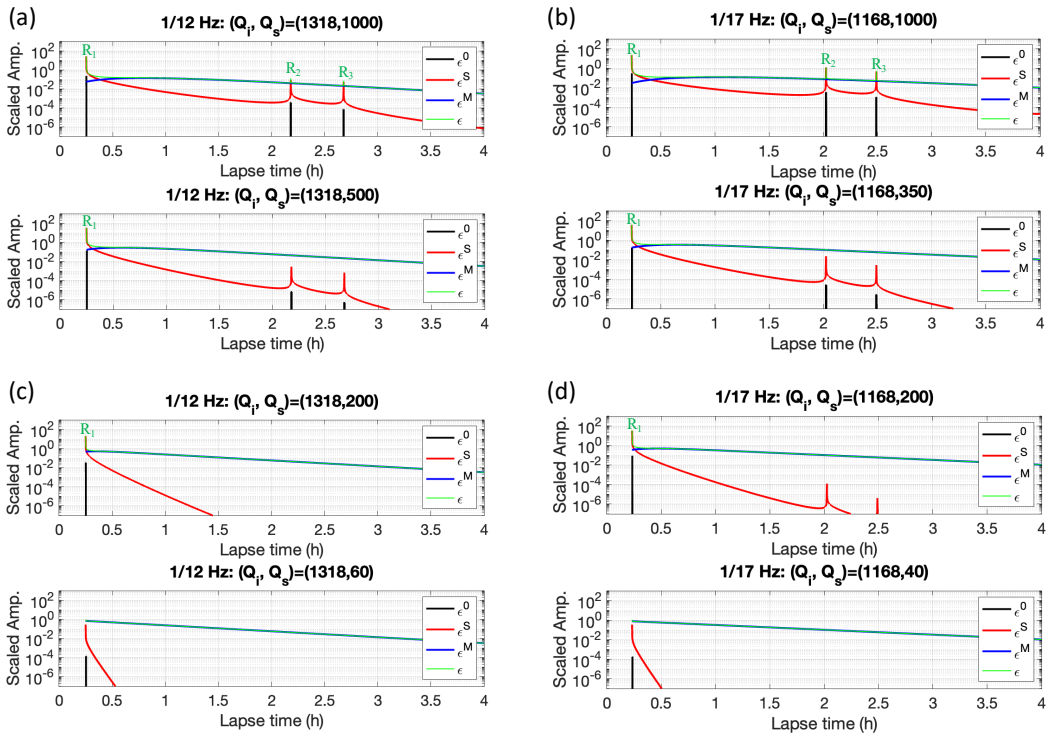

Figure 4. (a)-(b) Examples of parameter study results for estimating the upper limit of Q_s at 1/12 Hz and 1/17 Hz. The black lines are the direct wave component, the red profile is the single-scattered component, the blue is the multiple-scattered component, and the green is the convolved profile. The first row is for Q_s = 1000, where the multi-orbital phases can be seen. The second row is the case for the upper limit of Q_s, where the contribution of the multiple scattering is strong enough to bury R_2 and the multi-orbital phases. (c)-(d) Examples of parameter study results for estimating the lower limit of Q_s at 1/12 Hz and 1/17 Hz. The first row is for Q_s = 200, where the R_1 phase can be confirmed. The second row is the case for the lower limit of Q_s, where the contribution of the multiple scattering is strong enough to bury the R_1 phase.

Lee et al. (2003) and Lee et al. (2006) estimated the terrestrial mantle Q_s using ScS wave scattering. They inverted for the Q_s using the Monte Carlo method based on the radiative transfer theory with the PREM's velocity and attenuation structure. Around 0.1 – 0.2 Hz in Figure 5b, we plotted the upper mantle value compatible with the upper limit of the lithospheric value at 1 Hz.

The volcanic region is known to be one of the most heterogeneous regions on Earth. Previous studies evaluated the scattering parameters in various volcanic areas using body waves generated by artificial seismic sources. For example, Wegler (2003) evaluated the Q_i and Q_s at Vesuvius volcano in Italy, Yamamoto and Sato (2010) assessed the quality factors at Asama volcano in Japan, and Prudencio et al. (2015) investigated Stromboli volcano in Italy. The complied parameter ranges are shown as the cyan areas in Figures 5a-b. When compared with the lithosphere, the volcanic area shows the smaller Q_i and Q_s, indicating the strong scattering and high attenuation rate.

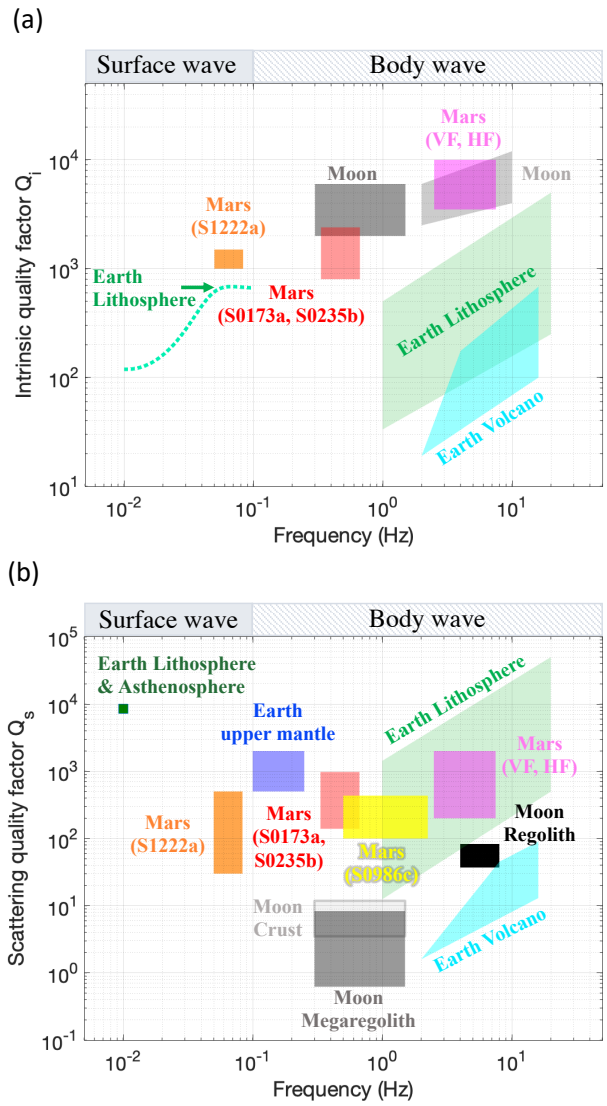

Figure 5. Comparison of (a) intrinsic quality factor and (b) scattering quality factor between the Earth, the Moon, and Mars. See Section 7 for the details.

7.2 Moon

The latest lunar intrinsic and scattering quality factors were evaluated by Blanchette-Guertin et al. (2012), Gillet et al. (2017), and Onodera et al. (2022).

Blanchette-Guertin et al. (2012) investigated the energy decay of the various types of moonquakes (such as deep moonquakes, shallow moonquakes, natural impacts, and artificial impacts) at different frequency bands, and systematically assessed the decay time and coda Q (Q_c). Under the intense scattering conditions, Q_c can be regarded as the S-wave Q_i [e.g., Yoshimoto and Jin (2008)]. In this study, assuming their Q_c estimation as Q_i, we show the corresponding Q_i range as dark and light grey areas in Figure 5a. The Q_i ranges from 2000 to 6000 in the middle frequency (0.3 – 1.5 Hz). Moreover, Q_i in the high frequency (2 – 10 Hz) takes a value of 2500 – 6000 at 2 Hz and 4000 – 12000 at 10 Hz, showing frequency dependence.

Regarding the scattering quality factors (black and grey areas in Figure 5b), Gillet et al. (2017) estimated the global Q_s by introducing the spherically layered geometry in the diffusion model. In Figure 5b, the crustal value (3.5 – 12) is presented as the light grey area. Nakamura (1976) evaluated the diffusivity of the regolith (surface fine and porous layer) as (6.2±0.2) $\times 10^{-3}$ km^2/s. It should be noted that we divided his estimation by 4 because the diffusivity in Nakamura (1976) was defined differently from that ordinally used. Using the corrected diffusivity, we estimated the regolith's Q_s as 37 – 83 at 4 – 8 Hz (the black region in Figure 5b). For the megaregolith — the fractured structure due to continuous meteoroid impacts, Onodera et al. (2022) evaluated Q_s= 0.6 – 8.3 in the middle frequency (the dark grey area in Figure 5b) in a forward approach using full 3D seismic wave propagation simulation.

7.3 Mars

The initial estimation of the diffusivity and intrinsic attenuation were carried out by Lognonné et al. (2020) using both teleseismic events (S0173a and S0235b) and a regional marsquake (S0128a). As the results for S0128a are integrated with those of Menina et al. (2021), we briefly review the scattering parameters for S0173a and S0235b. Based on the radiative transfer modeling proposed by Margerin (2017), Lognonné et al. (2020) investigated the two teleseismic events. They estimated the diffusivity (200 – 700) and intrinsic quality factor (800 – 2400) at around 0.5 Hz. Here, we converted the diffusivity into the scattering Q (140 – 977). The red areas in Figures 5a-b correspond to their estimations.

Following the initial outcomes by Lognonné et al. (2020), Menina et al. (2021) evaluated the scattering and attenuation properties at higher frequencies ($>$ 2.4 Hz) using Very High Frequency (VF) and High Frequency (HF) events. They took over the approach of Lognonné et al. (2020) and estimated Q_i and Q_s as 3500 – 10000 and 200 – 2000, respectively (the magenta areas in Figures 5a-b). Recently, using the seismic waves generated by a meteoroid impact (S0986c), Garcia et al. (2022) gave an estimation of the crustal structure around the InSight landing site. We computed the diffusivity and scattering quality factor by referring to their supporting materials together with the diffusion model described by Strobach (1970). Consequently, we obtained Q_s = 100 – 435 at 0.5 – 2.25 Hz (yellow area in Figure 5b). At the low frequency ($<$ 0.1 Hz), this study provided the first estimation of Q_i and Q_s using the largest marsquake (S1222a) by applying the radiative transfer theory on a spherical Mars (orange area in Figures 5a-b).

7.4 Comparison of three solid bodies

Comparing the Martian Q_i with those of the Earth and the Moon, we found that the absorption feature coincided with the lunar one at the high frequency, whereas it turned into a more Earth-like value at the middle and low frequencies. On the other hand, the Martian scattering quality factor is in accordance with the Earth's lithosphere. These results are consistent with the general marsquake features. The event lasts a few tens of minutes, which is longer than earthquakes but not as long as moonquakes [e.g., Lognonné et al. (2020); Onodera et al. (2022)]. Furthermore, the Martian scattering is not as intense as the Moon, which makes the seismic phases identifiable like earthquakes. According to the quantitative comparison in Figures 5a-b, we can preliminarily conclude that the Martian absorption and scattering properties are more Earth-like rather than Moon-like.

8 Conclusion

In this study, we investigated the properties of seismic scattering and intrinsic absorption on Mars. In previous studies, these parameters were not constrained at frequen-

cies below 0.1 Hz. We provided initial estimations of the scattering and intrinsic Q at that frequency, focusing on the long-lasting surface wave coda observed in the S1222a marsquake. Using the radiative transfer theory on a spherical Mars, we succeeded in modeling the observed seismic coda features. As a result, we found $Q_i = 1000 - 1500$ and $Q_s = 30 - 500$, respectively.

In the comparison of the Martian quality factors derived so far with other solid bodies, we found that the overall scattering and absorption features of Mars appear similar to that of the Earth. Because the current estimation is building on only a small portion of the detected marsquakes, we hope that future works will update our results through more systematic and thorough analyses to better illustrate the heterogeneous structure inside the red planet.

Data availability

The SEIS data from the InSight mission used in this study can be retrieved through InSight Mars SEIS Data Service (2019) and InSight Marsquake Service (2022). A sample code for downloading data from the IRIS web server can be found at Onodera (2022).

Acknowledgments

We acknowledge NASA, CNES, their partner agencies and Institutions (UKSA, SSO, DLR, JPL, IPGP-CNRS, ETHZ, IC, and MPS- MPG), and the flight operations team at JPL, SISMOC, MSDS, IRIS-DMC, and PDS for acquiring and providing InSight data, including SEED SEIS data. This is InSight contribution number 313.

References

Aki, K. (1969). Analysis of the seismic coda of local earthquakes as scattered waves. *Journal of Geophysical Research (1896-1977)*, *74*(2), 615-631. doi: https://doi.org/10.1029/JB074i002p00615

Aki, K., & Chouet, B. (1975). Origin of coda waves: Source, attenuation, and scattering effects. *Journal of Geophysical Research (1896-1977)*, *80*(23), 3322-3342. doi: https://doi.org/10.1029/JB080i023p03322

Banerdt, W. B., Smrekar, S. E., Banfield, D., Giardini, D., Golombek, M., Johnson, C. L., ... Wieczorek, M. (2020). Initial results from the insight mission on mars. *Nature Geoscience*, *13*(3), 183-189. doi: 10.1038/s41561-020-0544-y

Blanchette-Guertin, J.-F., Johnson, C. L., & Lawrence, J. F. (2012). Investigation of scattering in lunar seismic coda. *Journal of Geophysical Research: Planets*, *117*(E6). doi: https://doi.org/10.1029/2011JE004042

Dziewonski, A. M., & Anderson, D. L. (1981). Preliminary reference earth model. *Physics of the Earth and Planetary Interiors*, *25*(4), 297-356. doi: https://doi.org/10.1016/0031-9201(81)90046-7

Garcia, R. F., Daubar, I. J., Beucler, É., Posiolova, L. V., Collins, G. S., Lognonné, P., ... Banerdt, W. B. (2022). Newly formed craters on mars located using seismic and acoustic wave data from insight. *Nature Geoscience*, *15*(10), 774-780. doi: 10.1038/s41561-022-01014-0

Giardini, D., Lognonné, P., Banerdt, W. B., Pike, W. T., Christensen, U., Ceylan, S., ... Yana, C. (2020). The seismicity of mars. *Nature Geoscience*, *13*, 205-212. doi: 10.1038/s41561-020-0539-8

Gillet, K., Margerin, L., Calvet, M., & Monnereau, M. (2017). Scattering attenuation profile of the moon: Implications for shallow moonquakes and the structure of the megaregolith. *Physics of the Earth and Planetary Interiors*, *262*, 28-40. doi: https://doi.org/10.1016/j.pepi.2016.11.001

Golombek, M., Williams, N., Warner, N. H., Parker, T., Williams, M. G., Daubar,

I., ... Sklyanskiy, E. (2020). Location and setting of the mars insight lander, instruments, and landing site. *Earth and Space Science*, *7*(10), e2020EA001248. (e2020EA001248 2020EA001248) doi: https://doi.org/10.1029/2020EA001248

InSight Mars SEIS Data Service. (2019). *SEIS raw data, InSight mission.* IPGP, JPL, CNES, ETHZ, ICL, MPS, ISAE-Supaero, LPG, MFSC. doi: 10.18715/SEIS.INSIGHT.XB_2016

InSight Marsquake Service. (2022). *Mars Seismic Catalogue, InSight Mission; V12 2022-10-01.* ETHZ, IPGP, JPL, ICL, Univ. Bristol. doi: 10.12686/A18

Karakostas, F., Schmerr, N., Maguire, R., Huang, Q., Kim, D., Lekic, V., ... Banerdt, B. (2021). Scattering Attenuation of the Martian Interior through Coda-Wave Analysis. *Bulletin of the Seismological Society of America*, *111*(6), 3035-3054. doi: 10.1785/0120210253

Kawamura, T., Clinton, J. F., Zenhäusern, G., Ceylan, S., Horleston, A. C., Dahmen, N. L., ... Banerdt, W. B. (2022). S1222a - the largest marsquake detected by insight. *Geophysical Research Letters*, e2022GL101543. doi: https://doi.org/10.1029/2022GL101543

Khan, A., Ceylan, S., van Driel, M., Giardini, D., Lognonné, P., Samuel, H., ... Banerdt, W. B. (2021). Upper mantle structure of mars from insight seismic data. *Science*, *373*(6553), 434-438. doi: 10.1126/science.abf2966

Kim, D., Banerdt, W. B., Ceylan, S., Giardini, D., Lekić, V., Lognonné, P., ... Panning, M. P. (2022). Surface waves and crustal structure on mars. *Science*, *378*(6618), 417-421. doi: 10.1126/science.abq7157

Knapmeyer-Endrun, B., Panning, M. P., Bissig, F., Joshi, R., Khan, A., Kim, D., ... Banerdt, W. B. (2021). Thickness and structure of the martian crust from insight seismic data. *Science*, *373*(6553), 438-443. doi: 10.1126/science.abf8966

Lee, W. S., Sato, H., & Lee, K. (2003). Estimation of s-wave scattering coefficient in the mantle from envelope characteristics before and after the scs arrival. *Geophysical Research Letters*, *30*(24). doi: https://doi.org/10.1029/2003GL018413

Lee, W. S., Sato, H., & Lee, K. (2006). Scattering coefficients in the mantle revealed from the seismogram envelope analysis based on the multiple isotropic scattering model. *Earth and Planetary Science Letters*, *241*(3), 888-900. doi: https://doi.org/10.1016/j.epsl.2005.10.035

Lognonné, P., Banerdt, W. B., Giardini, D., Pike, W. T., Christensen, U., Laudet, P., ... Wookey, J. (2019). Seis: Insight's seismic experiment for internal structure of mars. *Space Science Reviews*, *215*(1), 12. doi: 10.1007/s11214-018-0574-6

Lognonné, P., Banerdt, W. B., Pike, W. T., Giardini, D., Christensen, U., Garcia, R. F., ... Zweifel, P. (2020). Constraints on the shallow elastic and anelastic structure of mars from insight seismic data. *Nature Geoscience*, *13*(3), 213-220. doi: 10.1038/s41561-020-0536-y

Maeda, T., Sato, H., & Ohtake, M. (2006). Constituents of vertical-component coda waves at long periods. *pure and applied geophysics*, *163*(2), 549-566. doi: 10.1007/s00024-005-0031-9

Margerin, L. (2017). Computation of green's function of 3-d radiative transport equations for non-isotropic scattering of p and unpolarized s waves. *Pure and Applied Geophysics*, *174*(11), 4057-4075. doi: 10.1007/s00024-017-1621-z

Masters, G., Woodhouse, J., & Freeman, G. (2011). *Mineos v1.0.2 [software].* Computational Infrastructure for Geodynamics.

Menina, S., Margerin, L., Kawamura, T., Lognonné, P., Marti, J., Drilleau, M., ... Banerdt, W. B. (2021). Energy Envelope and Attenuation Characteristics of High-Frequency (HF) and Very-High-Frequency (VF) Martian Events. *Bulletin of the Seismological Society of America*, *111*(6), 3016-3034. doi: 10.1785/0120210127

Nakamura, Y. (1976). Seismic energy transmission in the lunar surface zone determined from signals generated by movement of Lunar Rovers. *Bulletin of the Seismological Society of America*, *66*(2), 593-606. doi: 10.1785/BSSA0660020593

Onodera, K. (2022). *Access to scientific data obtained by NASA's Mars exploration mission "InSight".* Researchmap. Retrieved from `https://researchmap.jp/blogs/blog_entries/view/809479/d29ec3b7f0fdd5a15a3be04ec97dc762?frame_id=1470639`

Onodera, K., Kawamura, T., Tanaka, S., Ishihara, Y., & Maeda, T. (2022). Quantitative evaluation of the lunar seismic scattering and comparison between the Earth, Mars, and the Moon. *Journal of Geophysical Research: Planets*, e2022JE007558. doi: https://doi.org/10.1029/2022JE007558

Prudencio, J., Del Pezzo, E., Ibáñez, J. M., Giampiccolo, E., & Patané, D. (2015). Two-dimensional seismic attenuation images of stromboli island using active data. *Geophysical Research Letters*, *42*(6), 1717-1724. doi: https://doi.org/10.1002/2015GL063293

Sato, H. (1977). Energy propagation including scattering effects sengle isotropic scattering approximation. *Journal of Physics of the Earth*, *25*(1), 27-41. doi: 10.4294/jpe1952.25.27

Sato, H. (2019). Isotropic scattering coefficient of the solid earth. *Geophysical Journal International*, *218*(3), 2079-2088. doi: 10.1093/gji/ggz266

Sato, H., Fehler, M. C., & Maeda, T. (2012). *Seismic wave propagation and scattering in the heterogeneous earth: Second edition.* Springer Berlin, Heidelberg. doi: 10.1007/978-3-642-23029-5

Sato, H., & Nishino, M. (2002). Multiple isotropic-scattering model on the spherical earth for the synthesis of rayleigh-wave envelopes. *Journal of Geophysical Research: Solid Earth*, *107*(B12), ESE 7-1-ESE 7-9. doi: https://doi.org/10.1029/2001JB000915

Sato, H., & Nohechi, M. (2001). Envelope formation of long-period rayleigh waves in vertical component seismograms: Single isotropic scattering model. *Journal of Geophysical Research: Solid Earth*, *106*(B4), 6589-6594. doi: https://doi.org/10.1029/2000JB900383

Scholz, J.-R., Widmer-Schnidrig, R., Davis, P., Lognonné, P., Pinot, B., Garcia, R. F., ... Banerdt, W. B. (2020). Detection, analysis, and removal of glitches from insight's seismic data from mars. *Earth and Space Science*, *7*(11), e2020EA001317. (e2020EA001317 10.1029/2020EA001317) doi: https://doi.org/10.1029/2020EA001317

Strobach, K. (1970). Scattering of seismic waves and lunar seismograms. *J. Geophys.*, *36*, 643–645.

Stähler, S. C., Khan, A., Banerdt, W. B., Lognonné, P., Giardini, D., Ceylan, S., ... Smrekar, S. E. (2021). Seismic detection of the martian core. *Science*, *373*(6553), 443-448. doi: 10.1126/science.abi7730

Wegler, U. (2003). Analysis of multiple scattering at vesuvius volcano, italy, using data of the tomoves active seismic experiment. *Journal of Volcanology and Geothermal Research*, *128*(1), 45-63. (Putting Volcano Seismology in a Physical Context. In memory of Bruno Martinelli) doi: https://doi.org/10.1016/S0377-0273(03)00246-4

Wu, R.-S. (1985). Multiple scattering and energy transfer of seismic waves — separation of scattering effect from intrinsic attenuation — I. Theoretical modelling. *Geophysical Journal International*, *82*(1), 57-80.

Yamamoto, M., & Sato, H. (2010). Multiple scattering and mode conversion revealed by an active seismic experiment at asama volcano, japan. *Journal of Geophysical Research: Solid Earth*, *115*(B7). doi: https://doi.org/10.1029/2009JB007109

Yoshimoto, K., & Jin, A. (2008). Chapter 10 coda energy distribution and attenu-

459 ation. In *Earth heterogeneity and scattering effects on seismic waves* (Vol. 50,
460 p. 265-299). Elsevier. doi: https://doi.org/10.1016/S0065-2687(08)00010-1

Figure1.

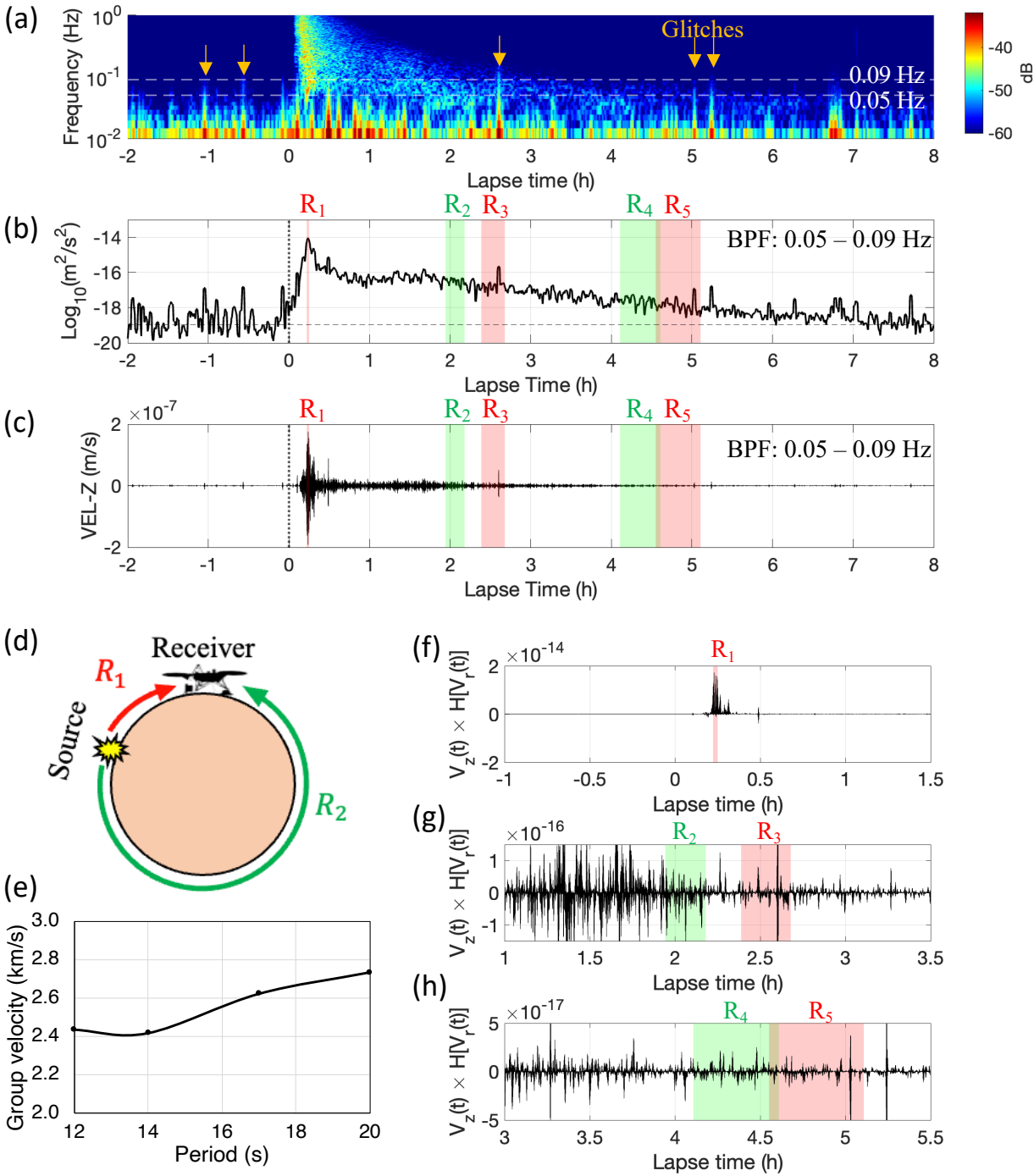
(a)
Frequency (Hz)
Glitches
0.09 Hz
0.05 Hz
dB
Lapse time (h)
(b)
R1
R2
R3
R4
R5
BPF: 0.05 – 0.09 Hz
Log10(m2/s2)
Lapse Time (h)
(c)
VEL-Z (m/s)
BPF: 0.05 – 0.09 Hz
Lapse Time (h)
(d)
Receiver
Source
R1
R2
(e)
Group velocity (km/s)
Period (s)
(f)
Vz(t) × H[Vr(t)]
Lapse time (h)
(g)
Vz(t) × H[Vr(t)]
Lapse time (h)
(h)
Vz(t) × H[Vr(t)]
Lapse time (h)

Figure2.

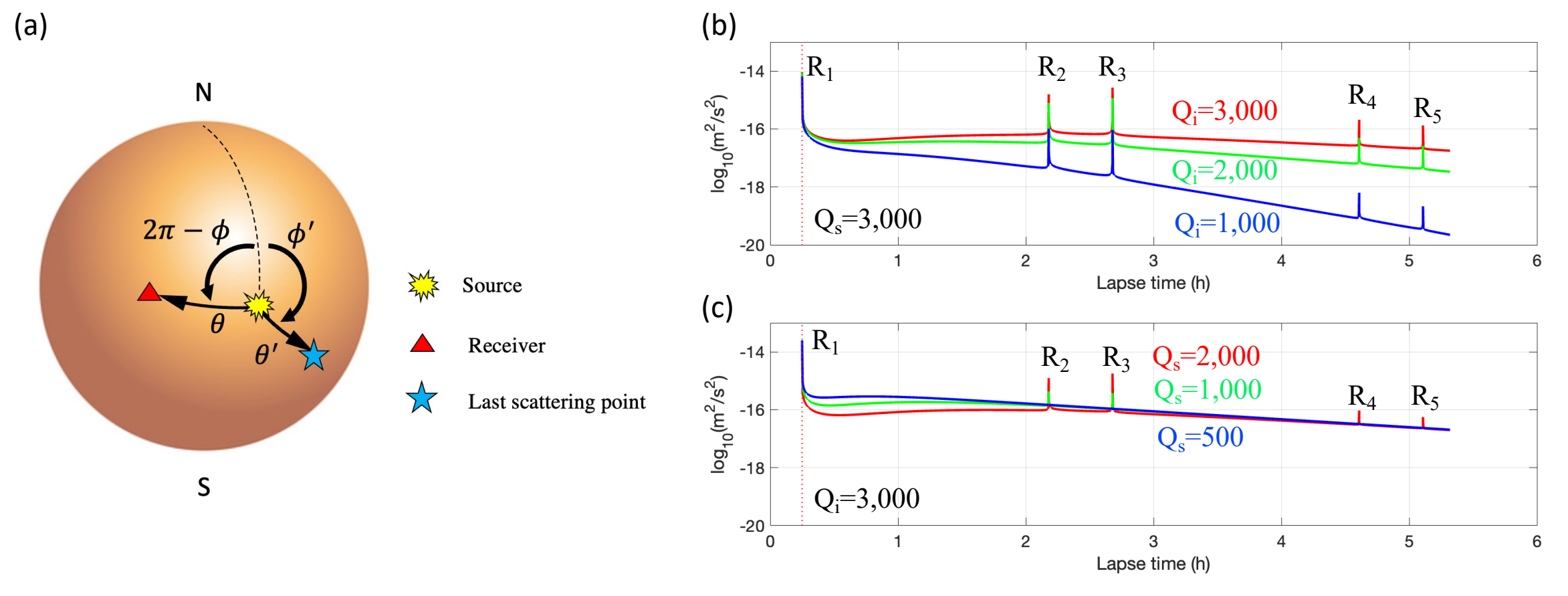
(a)
N
S
$2\pi - \phi$
ϕ'
θ
θ'
Source
Receiver
Last scattering point
(b)
R_1
R_2
R_3
R_4
R_5
Q_i=3,000
Q_i=2,000
Q_i=1,000
Q_s=3,000
$\log_{10}(m^2/s^2)$
Lapse time (h)
(c)
R_1
R_2
R_3
R_4
R_5
Q_s=2,000
Q_s=1,000
Q_s=500
Q_i=3,000
$\log_{10}(m^2/s^2)$
Lapse time (h)

Figure3.

(a) Residual map

(b) Best-fitted curve

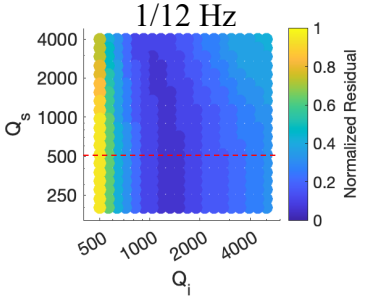

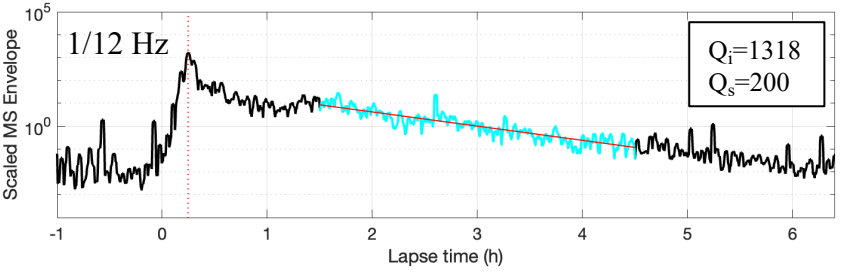

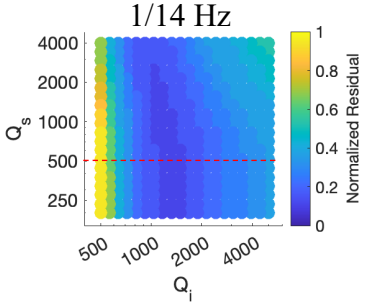

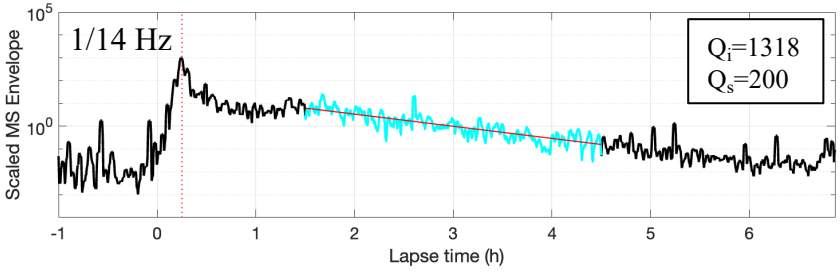

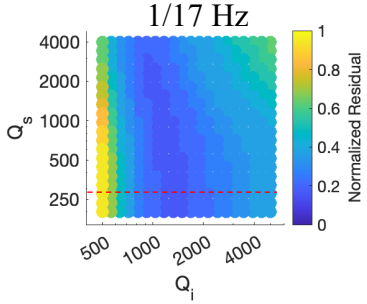

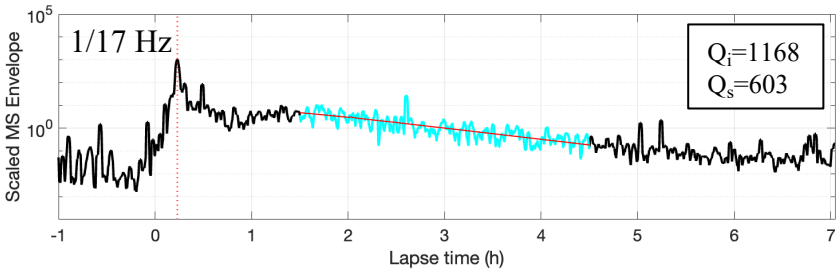

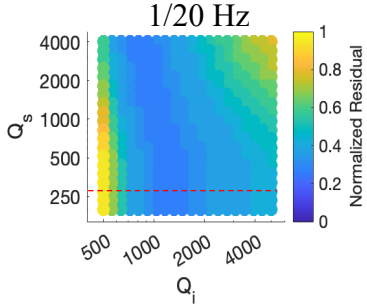

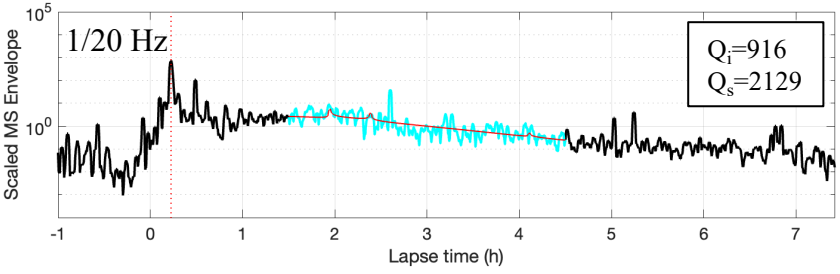

Figure4.

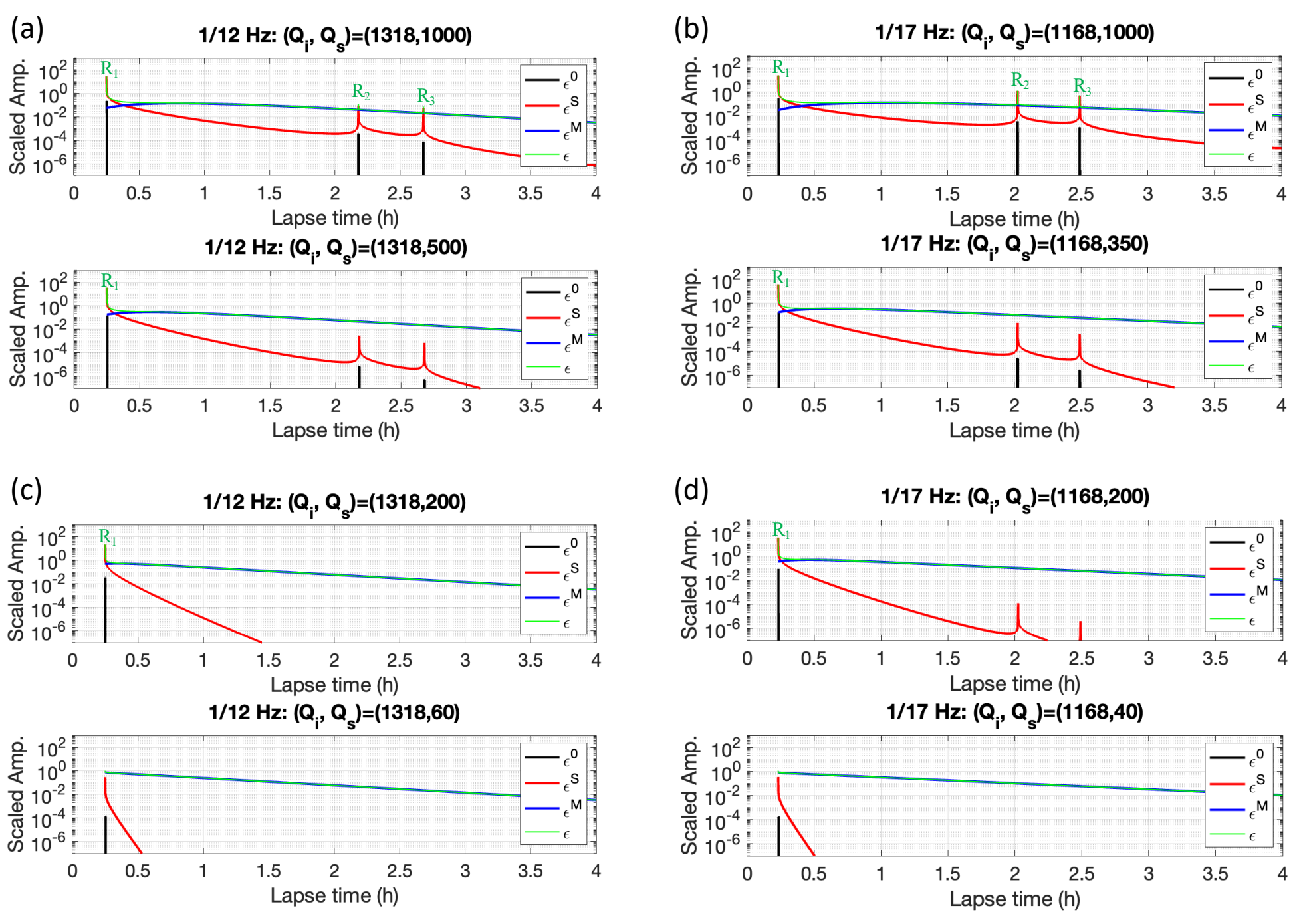
(a)
1/12 Hz: (Q_i, Q_s)=(1318,1000)
1/12 Hz: (Q_i, Q_s)=(1318,500)
(b)
1/17 Hz: (Q_i, Q_s)=(1168,1000)
1/17 Hz: (Q_i, Q_s)=(1168,350)
(c)
1/12 Hz: (Q_i, Q_s)=(1318,200)
1/12 Hz: (Q_i, Q_s)=(1318,60)
(d)
1/17 Hz: (Q_i, Q_s)=(1168,200)
1/17 Hz: (Q_i, Q_s)=(1168,40)
Scaled Amp.
Lapse time (h)
R1
R2
R3
ε0
εS
εM
ε

Figure5.

(a)

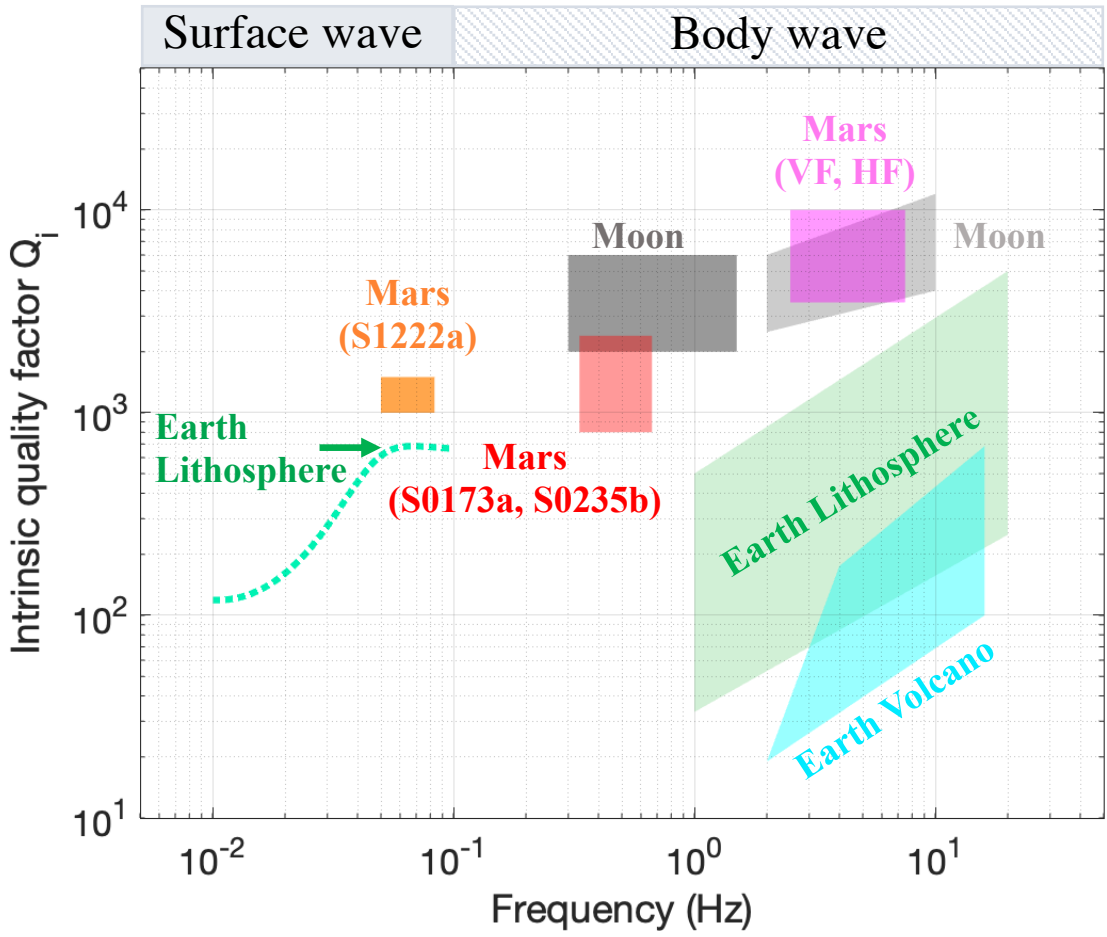
Surface wave
Body wave
Mars
(VF, HF)
Moon
Moon
Mars
(S1222a)
Earth
Lithosphere
Mars
(S0173a, S0235b)
Earth Lithosphere
Earth Volcano
Intrinsic quality factor Q_i
10^4
10^3
10^2
10^1
10^{-2}
10^{-1}
10^0
10^1
Frequency (Hz)

(b)

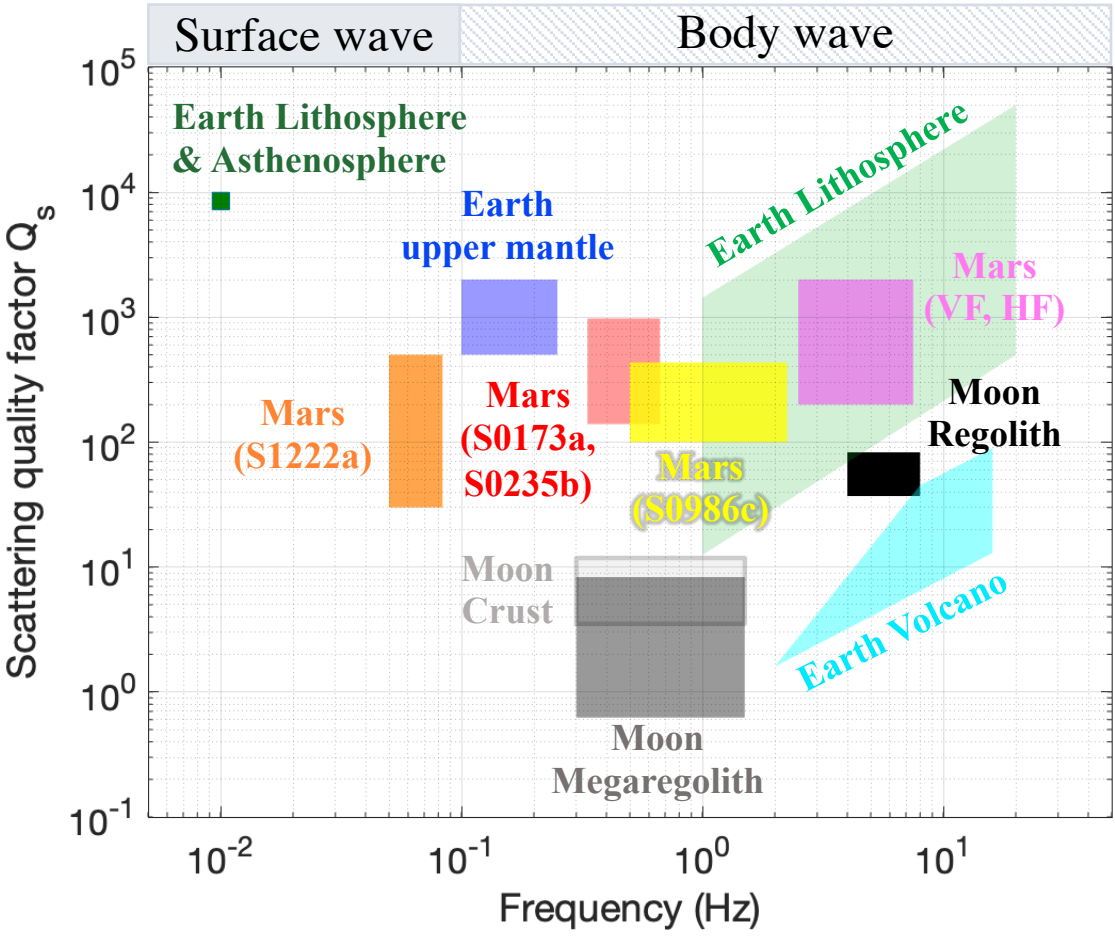
Surface wave
Body wave
Earth Lithosphere
& Asthenosphere
Earth
upper mantle
Earth Lithosphere
Mars
(VF, HF)
Mars
(S1222a)
Mars
(S0173a,
S0235b)
Mars
(S0986c)
Moon
Regolith
Moon
Crust
Earth Volcano
Moon
Megaregolith
Scattering quality factor Q_s
10^5
10^4
10^3
10^2
10^1
10^0
10^{-1}
10^{-2}
10^{-1}
10^0
10^1
Frequency (Hz)